Detection and analysis of mass wasting events in chalk sea cliffs using UAV photogrammetry

Article (Accepted Version)

Detection and analysis of mass wasting events in chalk sea cliffs using UAV photogrammetry

Jamie Gilham, John Barlow and Roger Moore

Department of Geography, University of Sussex, Brighton, UK

Abstract

Coastal cliff recession represents a significant risk to both people and infrastructure, it is therefore important that we are able to efficiently monitor these environments to inform future management decisions. Through the use of UAV digital photogrammetry, we obtain point clouds to develop monthly models of the sea cliffs at Telscombe, East Sussex, UK between August 2016 and July 2017. The models captured were accurate to 0.05 m and had an average point density of 351 pts/m^2. Using the methodology presented we were able to automatically detect rockfalls by undertaking a 2.5D surface change detection which populated monthly inventories through volumetric estimations. A total of 10,085 failures were observed with an estimated volumetric flux of 3,889.4 m^3 over the 12 month period of data collection. Due to the high frequency of data capture, successive block failures in the Newhaven Chalk formation were observed. The largest failure within the 12 month period was estimated at 2,546.8 m^3 and followed significant toe erosion due to wave action. The steepening of the cliff face was modelled through limit equilibrium analysis to determine the reduction in factor of safety for the months preceding failure. We then present a magnitude-frequency analysis using negative power laws from the monthly rockfall inventories for the entire study area. The negative power law models produced a strong correlation across all months with r^2 values ranging from 0.97 to 0.99. The normalised power law scaling parameters ranged from 1.421 to 1.955 for β and from 33.79 to 904.14 for s. The observed rollover in power laws presented in previous research matches the resolution of the data presented in this study. Our results show that this method of data capture is comparable to existing methods whilst offering significant benefits in field surveying time and cost.

Keywords: UAV photogrammetry, coastal cliff, 2.5D surface change detection

1. Introduction

Recent advancement in spatial data acquisition (Buckley et al., 2008) has seen greater attention given to the evolution of sea cliffs in the research literature (Lee et al., 2001; Trenhaile, 2002; Dong & Guzzetti, 2005; Treixeira, 2006; Lim et al., 2010; Hurst et al., 2016). Obtaining digital surface models had been dominated by the use of airborne light detection and ranging (LiDAR) (Haala & Rothermel, 2012; Gonçlaves & Henriques, 2015). Terrestrial laser scanning (TLS) was the first of these acquisition advances, which enabled the plane of interest to be altered from the typical downward looking aircraft sensors to obtain high precision data of near vertical slopes from the required perspective. However, this method placed restrictions on the spatial extent of data capture in coastal locations due to limitations imposed on collecting data terrestrially from the foreshore (Rosser et al., 2005). Mobile LiDAR data acquisitions enabled studies in complex geomorphological environments or specific study sites to be undertaken (Lumme et al., 2008; Kukko et al., 2012; Glennie et al., 2013; Michoud et al., 2015), however these systems are usually very expensive although the cost of UAV mounted LiDAR has reduced recently. One drawback of mobile deployments in the form of vehicle mounted LiDAR using paths along the base of cliff environments is the disadvantageous capture geometry, which results in a high density of points at the base of cliff and a low density of points at the cliff top. The emergence of unmanned aerial vehicles (UAVs) alongside the relative affordability and the technological advances in small and medium format digital cameras (Graham & Koh, 2002; Westoby et al., 2012) has provided an alternative platform for data capture. Various photogrammetry software platforms exist (Hugenholtz et al., 2013) which can generate models of similar accuracies to TLS whilst reducing survey time and cost. For these reasons, terrestrial and automated aerial photogrammetry have become an influential tool in the advancement of remote sensing for three dimensional topographic modelling (Huang, 2000; Lim, 2006; Remondino & El-Hakim, 2006; Matthews, 2008; Eisenbeiß, 2009; Fraser & Cronk, 2009; Lim, 2014; Barlow et al., 2017). The method has advanced significantly in recent years with the development of soft copy triangulation and image based terrain extraction algorithms (Westoby et al., 2012) which has enhanced the data and model outputs formulated from stereo-pairs. Many applications of UAV digital photogrammetry have used

structure from motion (SfM) which requires multiple passes, with images captured at varying angles and ranges to automatically produce a bundle adjustment which is used to calibrate the camera lens and locate points in space which can later be assigned a coordinate system (Westoby et al., 2012). However, for this study a more traditional photogrammetry approach was undertaken using a calibrated camera and strip photography in order to maximise the spatial extent of the dataset and improve efficiency. This approach reduces the amount of images required for data processing and does not require the array of viewing angles required in SfM (e.g. James & Robson, 2012) to produce a reliable calibration from the images captured from the surveys.

The ability to capture both high frequency and high precision data of the coastal cliff environment has improved over the last decade (Rosser et al., 2005; Lim et al., 2010; Barlow et al., 2012). By obtaining sequential datasets (Kuhn & Prüfer, 2014; Cook, 2017; Medjkane et al., 2018) at regular intervals 2.5D surface change detection (Rosser et al., 2005) enables researchers to observe the iterative process of toe erosion or the precursors to larger failures within the coastal cliff environment. With the development of UAV capabilities larger sections of coast can be captured than in previous TLS or terrestrial photogrammetry studies (Lim et al., 2010; Barlow et al., 2012) whilst offering comparable accuracy and resolution of the data (Barlow et al., 2017). This research presents the UAV photogrammetry methodology for collecting high precision data and the subsequent analysis undertaken to quantify and determine the erosional cycle of mass wasting events in chalk sea cliffs.

2. Study site

Telscombe cliffs are located in East Sussex, UK (Figure 1) and form one of the few unprotected sections of coastline between Brighton and Newhaven**.** The cliffs are formed of Cretaceous Chalk, predominately of the Newhaven formation although there are small outcrops of the Culver formation. The site is approximately 750 m in length with dry valleys at either end of the cliffs (Mortimore, 1997). The cliffs are orientated to the south-west with the maximum elevation approximately 49 m centrally in the study area. The dominant wave direction is from the south-west (May, 2003). A shingle beach protects the cliff toe of the eastern portion of the site and tapers over 300-350 m (Figure 1). To the

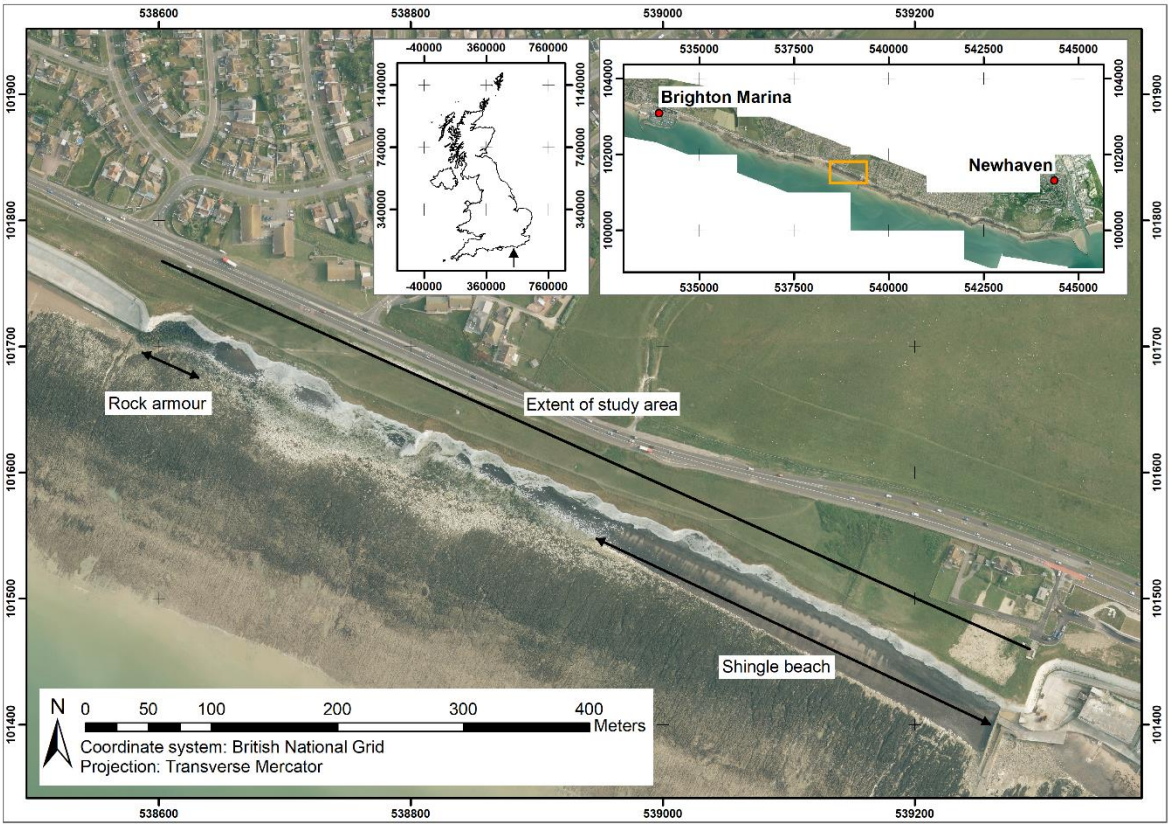

Figure 1: Study area of Telscombe cliffs, East Sussex, UK (2013 aerial imagery downaloaded from the CCO).

Figure 2: Telscombe cliffs, East Sussex. (Image: Author's own, captured from the shore platform).

78 west, rock armour prevents outflanking of the sea wall and promenade for approximately 50 m. The

average spring tidal range at Telscombe is 6.1 m (CCO, 2015) which enables interaction of waves with the base of cliff at high tide. The Newhaven Chalk cliffs at Telscombe (Figure 2) are characterised by steeply inclined conjugate joints sets which result in a pyramidal cliff morphology (Mortimore et al., 2004). Successive block failures occur along conjugate discontinuity joint sets with the most favourable mechanisms of failure being wedge (Mortimore et al., 2004; Barlow et al., 2017) and planar. These geological controls alongside various bedding planes determine the magnitude of failure along this section of cliff line.

3. Methods

This study captured monthly datasets to produce 3D models of the Telscombe cliffs using UAV photogrammetry. A 2.5D change detection was undertaken by comparing the sequential models to estimate the volumetric flux of the observed mass movements.

3.1. UAV photogrammetry data capture

High precision models were generated through digital photogrammetry using a Nikon D810 camera with an AF Nikkor 24 mm f/2.8D lens mounted on a DJI S1000 octocopter. The Nikon D810 is a full frame camera with a sensor size of 35.9 x 24 mm, image size of 7360 x 4912 pixels (36 Mpix) and a pixel pitch of ≈ 4.9 µm. Given the sensor size and 24 mm focal length lens the angular field of view was H: 73.6° (1.28 rad) x V: 53.1° (0.93 rad). Camera settings were optimised for flight speed and environmental conditions with an aperture of f/8, a shutter speed of 1/5000 seconds and ISO which varied from 800-1600. These settings were selected in the field, to account for the natural lighting conditions encountered for each survey and to replicate the image quality under the optimum static capture settings of ISO 100, aperture priority and manual focus mode (ADAM Technology, 2010). In order to minimize motion blur, the UAV was set to a constant speed of 3 ms^{-1} such that the camera only moved 0.6 mm during each exposure. Each survey typically consisted of 54 landscape images containing the entire cliff, captured automatically at 5 second intervals. The camera was set orthogonal to the cliff face with the aid of live streaming video (Barlow et al., 2017) and followed an

automated flight path which maintained a distance of 50 m from the cliff and flight altitude of 21 m (mid cliff height). At this distance, the camera and lens configuration has a field of view of 93 x 54.5 m, a nominal photograph scale of 1:2.083 and the image pixels represent a ground sampling distance of 10.2 mm (Wenzel et al., 2013). The strip photography is the best capture method available for such large sections of cliff line with a pre-calibrated short focal length camera at a relatively close distance (Birch, 2006) and resulted in an approximate image overlap of 80%. The total flight time for each survey was 8 minutes, which is a significant reduction in data capture time in comparison to laser scanning methods.

3.1.1. Camera calibration

An interior orientation or calibration was completed for the Nikon D810 AF Nikkor 24 mm f/2.8D using an alternative flight plan which included two strips, one pass at approximately 17 m elevation and the other at 25 m. Both image sets were captured orthogonal to, and focussed on, the centre of the cliff face, resulting in a convergent image set database. The flight path, speed and image capture settings remained as described previously, the resultant overlap of the images in the horizontal plane was therefore maintained at 80% and the vertical overlap of the cliff face was 100%. The fixed camera parameters of image size (pixels), sensor size (mm), lens camera and C (focal length) were required as pre-orientation data, all other interior orientation entries were left empty as these are populated automatically at a later stage. The generation of relative only points (ROPs), the ADAM 3DM terminology for pixel matching within images, forms the key automation process which has revolutionised digital photogrammetry through short processing-cycles (Konecny, 2003; Luhman et al., 2011). The generated ROPs were manually checked to remove any identified matching pixels which were found in either the limited areas of sky or within the foreground at the extremities of the image where the depth changes substantially within the image and there is no ground control (e.g. shore platform to cliff face).

128 Following the manual filtering of ROPs an image resection was required to derive the interior
129 orientation utilising the relative image points and the absolute GCPs (Linder, 2003). The image
130 resection process was implemented to determine an initial approximation of the ROPs in three
131 dimensional space (Birch, 2009). The approximated points were processed as a bundle adjustment
132 (Clifford et al., 2004), which refined the construction of the model through creation of jointly optimal
133 3D models (Luhman et al., 2011; 2013). An absolute stable calibration was achieved for the Nikon
134 D810 with AF Nikkor 24 mm f/2.8D with a 3DSE of 0.03 m and a calculated focal length of 24.25 mm.

135 Errors of residual 'doming' from imagery captured from a single strip plan (James & Robson, 2014;
136 James et al., 2017) are more pronounced in SfM models (James & Robson, 2014) where control and
137 check point measurements are typically more limited. The camera and lens distortion parameters
138 obtained from the convergent image set calibration provided a stable interior orientation used on a
139 single strip plan survey for the data collected in this study.

140 **3.1.2. Ground control network**

141 For the first survey, a ground control network consisting of 23 targets was installed at the
142 study site with 18 equidistantly spaced at the cliff toe with the remainder located at accessible cliff
143 top locations. The targets were black squares (21 cm x 21 cm) with a white circle in the centre (7 cm
144 in diameter), this was the optimal format of targets for the ADAM 3DM software. The software uses
145 an algorithm to automatically find the centre of the target to within 1/10 pixel. Cliff top coordinates
146 were obtained using dGPS whilst the cliff toe points were recorded through the use of a total station
147 to overcome the issue of 'shadowing', a common problem in obtaining dGPS coordinates in complex
148 terrain morphologies (Young, 2012). Four base station locations were surveyed using dGPS where the
149 total station was installed. Each total station survey covered a distance along the cliff toe of
150 approximately 190 m (a quarter of the survey area) and captured either four of five points. All
151 coordinates were accurate to 0.02 m in all planes. To reduce time in the field surveying and installing
152 ground control, a network of 30 flints were identified in the first 3D model. The coordinates of these

153 flints were extracted and used as the ground control network for all subsequent surveys, such that
154 targets were only required on the first survey. This approach reduces problematic issues such as 3D
155 point cloud deformation (Dewez et al., 2016). However, it must be noted that the static network of
156 flints is transient in that they can be lost in rockfalls. This can be partly addressed through careful
157 selection and introducing a lot of redundancy into the ground control network such that the loss of a
158 few points does not negatively influence 3D control.

159 **3.2. Model generation and 2.5D surface change detection**

160 All photogrammetry processing was undertaken in ADAM 3DM Mine Mapping Suite (Build
161 1488) which consisted of bundle adjustments, generation of epipolar images and point cloud
162 generation. The generated models produced a maximum overall 3D standard error of 0.05 m (Table
163 1). Error assessment found the greatest component residual error across all datasets was 0.10 m. The
164 largest component error coincided with the survey which captured two images less (52 instead of 54)
165 than the other surveys, this was as a result of wind conditions which increased the speed of the UAV
166 near the beginning of the December survey. Therefore, a threshold of 1 x $10^{-3}m^3$ was set as the

	Residuals (m)				
Month	**X**	**Y**	**Z**	**Standard Error**	**Max. Component Error**
August 2016	0.02	0.02	0.01	0.03	0.05
September 2016	0.02	0.02	0.01	0.03	0.05
October 2016	0.01	0.02	0.01	0.03	0.04
November 2016	0.03	0.03	0.01	0.05	0.06
December 2016	0.01	0.05	0.01	0.05	0.10
January 2017	0.04	0.02	0.04	0.05	0.08
February 2017	0.02	0.02	0.03	0.04	0.06
March 2017	0.01	0.03	0.02	0.03	0.06
April 2017	0.02	0.05	0.01	0.05	0.08
May 2017	0.03	0.03	0.02	0.05	0.06
June 2017	0.02	0.03	0.03	0.05	0.07
July 2017	0.03	0.03	0.02	0.05	0.07

Table 1: Exterior orientation component and overall accuracy for monthly UAV photogrammetry models from August 2016 to July 2017.

167 minimum reliable detectable rockfall volume (Di Maro et al., 2006; Dewez et al., 2013), which directly
168 relates to the greatest depth uncertainty (0.10 m) in the generated models (see below). This threshold
169 is comparable to that reported for studies using TLS (Rosser et al., 2005; Lim et al., 2010) and also

matches the rollover observed in the negative power law scaling of rockfalls presented by Barlow et al. (2012). The rollover in the distribution found for low magnitude events can be attributed to a sampling bias through an under counting of events below the 1 x 10^{-3} m^3 threshold. Point clouds had an average point density of 351 points/m^2 and were exported to CloudCompare where they were rotated so that the average dip direction of 204° was parallel to the Y plane such that measurements between models would represent true depth change. The point clouds were then rasterised with a cell size of 0.10 m and set to report the average depth value. A 2.5D surface change detection (Rosser et al., 2005) was undertaken on the raster datasets. An investigation into the cliff azimuth revealed a spatial variation of ±4° for planes best fit to 100 m sections of cliff face. The impact of this variation on the overall volumetric results was considered negligible. Furthermore, this method enabled automatic detection of rockfalls between sequential raster datasets, which significantly reduced processing time when populating the rockfall inventory.

The raster datasets were processed in ArcGIS to calculate surface and volumetric change. Surface difference models revealed change in vegetated areas, beach volume and edge effects, the latter of these were only visible along the edge of the buttresses at the toe of the cliff where there was an abrupt change in depth and only represented a narrow band of pixels (0.1 m – 0.2 m). The following method was developed to remove these issues and enable automatic detection of rockfalls. Each monthly dataset was subtracted from the initial state, August 2016. For any identified rockfall to be classified as real and not a result of one of the aforementioned issues (e.g. vegetated areas or beach material), the surface change would have to exist in two of these datasets. All of the monthly subtraction rasters (from the initial state), with the exception of July 2017, were reclassified to a binary dataset of surface change greater than 0.10 m equal to 1 and all other data set to 0. The August - July 2017 surface change model followed the same threshold of classification as the other datasets but change was reclassified to 10 and all other data as 0. The justification for this alteration is that true rockfalls would be visible in at least two months of data but as there is no comparative dataset for July, change must be classified differently or would be removed. The binary rasters were totalled and

196 any value less than 12 (change recorded in two datasets plus July) was reclassified to 0 and all values
197 greater than 12 were reclassified to 1, generating a mask which could be used to remove false change
198 from all the monthly datasets (e.g. Aug-Sep, Sep-Oct). This automated method reduced processing
199 time and meant that only the edge effects and vegetation from the July dataset had to be verified
200 against the images to determine if the change represented a rockfall. Finally, the mask was trimmed
201 to represent the extent of the cliff face and to remove the shore platform or beach material from the
202 rasters. All surface change below the detectable threshold was removed by masking the rasters for
203 each month and volumetric estimations were undertaken through raster analysis in ArcGIS.

204 **3.3. Negative power law scaling of rockfalls**

205 One of the conventional methods to assess erosion within geomorphic environments is through
206 magnitude-frequency analysis (Wolman & Miller, 1960; Stark & Guzzetti, 2009; Barlow et al., 2012;
207 Lim, 2014). Two types of negative power laws (Bak, 1996) have been used in the scientific literature
208 to assess the probability of landslide volumes; the first uses frequency or probability density (Brunetti
209 et al., 2009) and the second uses a cumulative complementary distribution function (Dussauge et al.,
210 2003; Dewez et al., 2013). This research uses frequency densities, which provide an estimate of the
211 production rate of each rockfall volume class, whilst the cumulative method provides a probabilistic
212 hazard estimate of exceeding a given volumetric threshold. The method used for this research has
213 previously been applied to the study of sea cliffs by Barlow et al. (2012) and Gilham et al (2018).

214 The negative power law scaling of rockfall magnitude-frequency distributions was modelled
215 using (Brunetti et al., 2009):

216 $$f(V_R)=sV_R^{-\beta} \quad (1)$$

217 where $f(V_R)$ is the frequency density, V_R is the magnitude of a given event and s and β are empirically
218 derived constants. This method has been frequently used in the scientific literature (Stark & Hovius,
219 2001; Dussauge et al., 2003; Brardinoni & Church, 2004; Guthrie & Evans, 2004; Malamud et al., 2004;

Dong & Guzzetti, 2005; Van Den Eeckhaut et al., 2007; White et al., 2008; Marques, 2008; Brunetti et al., 2009; Rossi et al., 2010) and has been found to be statistically robust over the volumetric range found in the rockfall inventory from Telscombe (Malamud et al., 2004; Barlow et al., 2012).

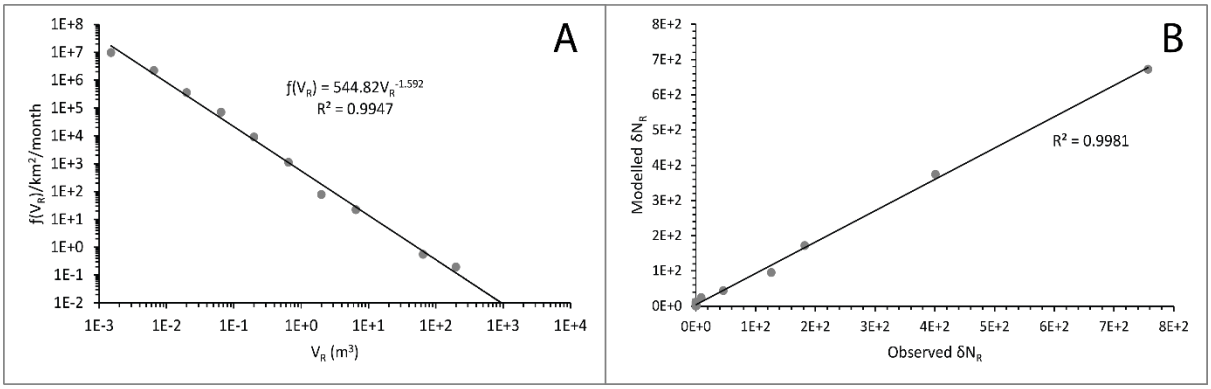

Figure 3: Power law estimation parameters for August to September 2016 (A) frequency density and magnitude of failures for the entire study area, (B) the predicted vs. observed frequency of failures for all binned data.

Rockfall magnitude-frequencies were plotted on logarithmic axes (Figure 3A) using traditional logarithmic binning methods (Guzetti et al., 2002; White et al., 2008; Barlow et al., 2012), the frequency densities were calculated for each of the classifications of rockfall magnitudes by using the formula (Malamud et al., 2004):

$$f(V_R) = \frac{\delta N_R}{\delta V_R} \quad (2)$$

where $f(V_R)$ is the frequency density of a rockfall with magnitude V_R, δN_R is the number of rockfalls within the specified volume range of δV_R, and δV_R corresponds to the width of the bin. The power law parameters are usually found using a least squares regression (LSR) method on logarithmically transformed data (Hovius et al., 1997; Korup, 2005; Barlow et al., 2012). The r^2 values for the regression analyses varied from 0.97 (April-May2017) to 0.99 (August-September 2016). The accuracy of the power law estimations were tested, following Barlow et al. (2012) using the integral of Equation 1:

$$\delta N_R = \int_{min}^{max} sV_R{}^{-\beta}\ dV_R \quad (3)$$

$$\delta N_R = \frac{sV_R{}_{max}^{1-\beta}}{1-\beta} - \frac{sV_R{}_{min}^{1-\beta}}{1-\beta} \quad (4)$$

By using Equation 4 and setting the $V_{R\,max}$ and $V_{R\,min}$ to the respective bin widths it is possible to assess the accuracy of the estimated power law parameters against the actual observations (Barlow et al., 2012), an example taken from the month August to September 2016 is provided in Figure 3B. The r^2 value of 0.9981 shows definitive agreement between the observations and the power law model. This provides confidence that the estimations reliably predict the frequency of the various magnitudes of failure. As the period between surveys varied the frequency densities were normalised by time and area (km^{-2} $month^{-1}$), with a month represented by 30.44 days (365.25 days per year / 12 months) and the area being 0.024km^2. During our analysis, cliff area was split into unprotected (0.014 km^2) and beach protected (0.01 km^2) sections. Importantly, the scale for normalising rockfalls both spatially and temporally varies through the literature, for example Hantz et al. (2003) used hm^{-2} yr^{-1} (cliff unit area) and Dewez et al. (2013) used km^{-1} yr^{-1}. This variation will affect the production rate value (s) between studies.

4. Results

The 2.5D surface change detection identified successive block failures in the Newhaven Chalk as presented by Mortimore et al. (2004) and also supplied evidence of the known process of toe erosion in inducing failure in coastal cliffs. A total volumetric flux of 3,889.4 m^3 was detected during the twelve month period of data collection with the largest failure between February and March 2017 at 2,546.8 m^3, although this figure does not account for erosion in the lower section of cliff which is obscured by debris (up to 10m high and 30m wide). The coordinate system used to present the results

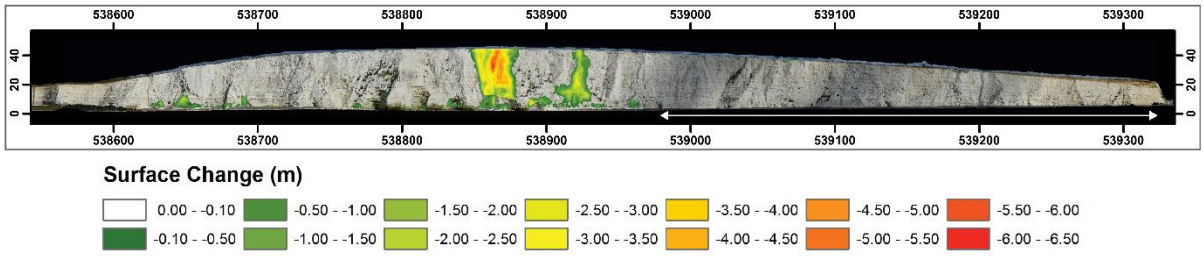

Figure 4: 2.5D surface change between August 2016 and March 2017 at Telscombe using UAV photogrammetry captured from the Nikon D810 with AF Nikkor 24mm f/2.8D lens, raster cell size=0.10 m (white line with arrows depicts extent of shingle beach).

was British National Grid (Figure 4, Figure 6 & Figure 8), and all references to failure locations, within

this section, are taken from the central point of the mass movement unless otherwise stated. The total number of failures observed was 10,085 with all of the larger failures occurring in the western half of the study area (Figure 4), this is unsurprising due to the shingle beach that acts as natural toe protection to the eastern section of the site. Given the total volume of the failures and the total surface area of the cliff an average recession rate can be calculated for the period of observations, for the entire site this was 0.165 m yr^{-1}. However, a more representative recession rate can be obtained by looking at the subsections of the study area, these were 0.279 m yr^{-1} for the unprotected cliff line and 0.002 m yr^{-1} for the cliff line fronted by the shingle beach. It is important to note that the observation period was only 12 months and so these figures may not be representative of the system over a longer time scale. These results agree with Lee (2008) who found at low beach levels there was high to extremely high recession with considerable variability in comparison to high beach levels where there was little to zero recession with limited variability. Although there was no investigation into beach volume or level during this study, there was a marked difference in the total volume of failures within each subsection; 3,872.62 m^3 for the unprotected and 16.73 m^3 for the section protected by the shingle beach.

As recession rates are deceptive metrics, the average depth/thickness of the failures were also investigated for each of the rockfall volume classifications used in the logarithmic binning (Figure 5).

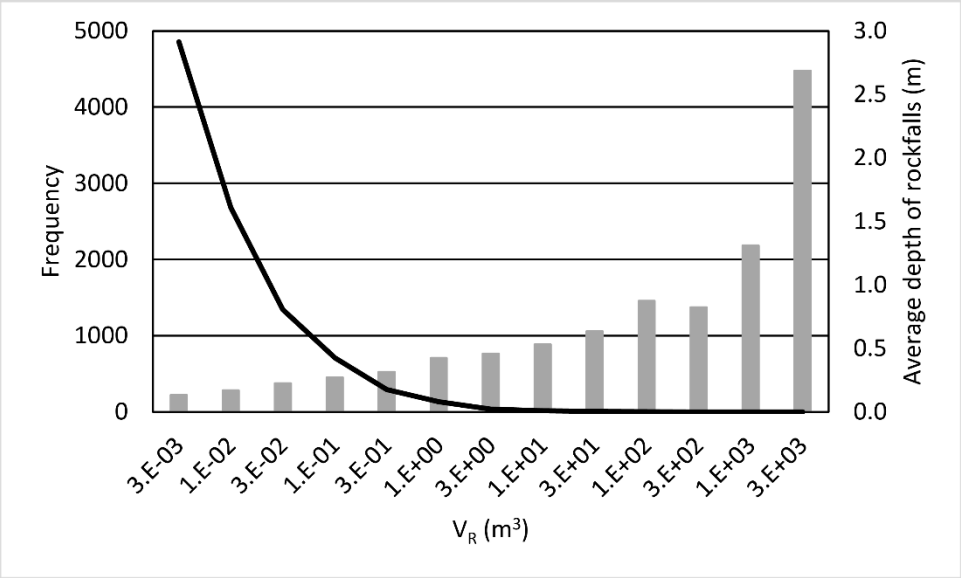

Figure 5: Average thickness and frequency of the logarithmically binned failure magnitudes (V_R).

As expected, the average thickness increased with the volume of failures with the largest failure reporting an average thickness of 2.69 m. The only exception to this trend was the average thickness for the range of 100 m^3 (1.E+02) – 300 m^3 (3.E+02), where the average thickness decreased from 0.875 m to 0. 825 m. This is likely explained by the frequency of failures within this classification, with only one failure recorded in each of the top three magnitudes throughout the study.

4.1. Successive block failures (August – December 2016)

The successive block failures identified in the cliffs at Telscombe occurred centrally (Figure 4 approx. 538920.00 m – Easting, 11.5 m to 37.7 m – Elevation) within the study area. Between August and December 2016 a total erosional mass flux of 788.20m^3 was recorded. The first failure occurred between data collection on the 5th August and 7th September 2016 (Figure 4 – 538915.81 m – Easting, 14.06 m – Elevation). Additional field visits during this period established the date of failure at between the 17th and 24th August. This window coincided with a two day period (20-21 August 2016) of strong south-westerly winds averaging 8.45ms^{-1}, with average peak gusts of 11.29 ms^{-1} and 19.2 ms^{-1} recorded respectively from the Brighton Marina meteorological station (Barlow et al., 2017), which is located approximately 5.5 km west of Telscombe. These strong winds coincided with the high tide, between 2.78 m and 3.38 m (Ordnance Datum) or 6.3 m and 6.9 m CD (Chart Datum). Waves that interacted with the base of the cliff during this period had a significant wave height (H_s) of 2.64 m, T_z of 5.16 seconds and azimuth of 230° resulting in substantial wave attack of the cliff toe (Barlow et al., 2017). The wedge failure, located centrally in Figure 6A (Figure 4 – 538915.81 m – Easting, 14.06 m – Elevation), failed on a conjugate joint set intersecting near the base of cliff. The failure was bound at the top by a band of more resistant nodular flint. The wedge failure volume was measured at 152.7 m^3. To the west of this failure the arch of a small cave failed (Figure 6A) during the same month with a volume of 47.2 m^3 (Figure 4 – 538897.38 m – Easting, 11.49 m – Elevation). The following month

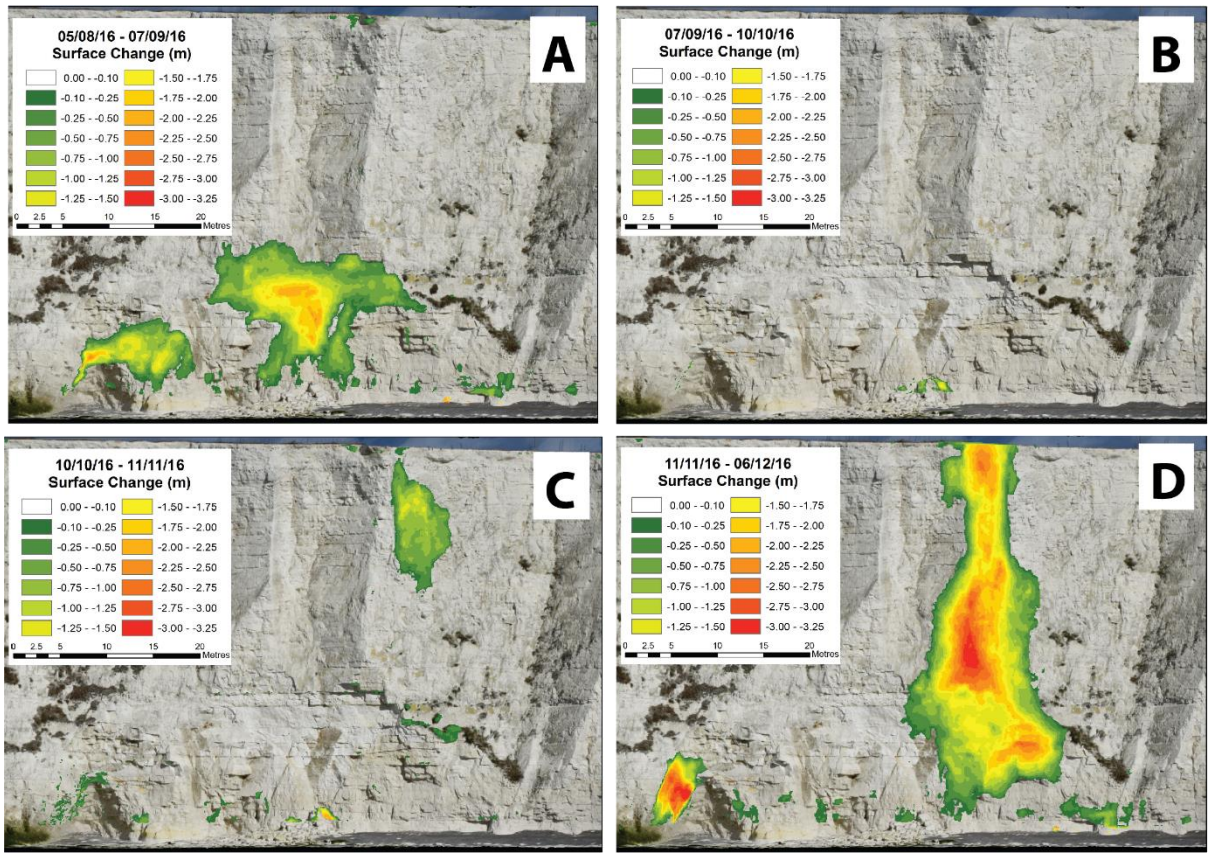

Figure 6: 2.5D surface change monitoring successive failures in the Newhaven Chalk at Telscombe between 05/08/16 and 06/12/16, cell size=0.10 m (A)Aug-Sep 2016, (B)Sep-Oct 2016, (C) Oct-Nov 2016 & (D) Nov-Dec 2016.

only revealed a relatively small amount of material, totalling 2.2 m^3, removed from the cliff toe (Figure 6B) before a block failed in the upper cliff between 10th October and the 11th November (Figure 6C), with a volume of 37.7 m^3 (Figure 4 – 538925.88 m – Easting, 37.78 m – Elevation). The preceding wedge failure led to an overhang of material for the upper two thirds of the cliff. This failed between the 11th November and the 6th December 2016 (Figure 6D) and was the largest of the failure blocks with a volume of 512.2 m^3 (Figure 4 – 538920.81 m – Easting, 29.43 m – Elevation). Further rockfall was identified around the arch, on the western side with a volume of 38.5 m^3 (Figure 4 – 538890.00 m – Easting, 10.35 m – Elevation). The progressive nature of these failures within the Newhaven Chalk was previously presented as a series of blocks which may fail either top down or bottom up on a series of conjugate shear surfaces by Mortimore et al. (2004). Mortimore et al.'s (2004) findings were based on a wealth of observations and knowledge acquired on the chalk coasts of Sussex, the results presented in Figure 6 offers clear supporting evidence illustrating this accepted process.

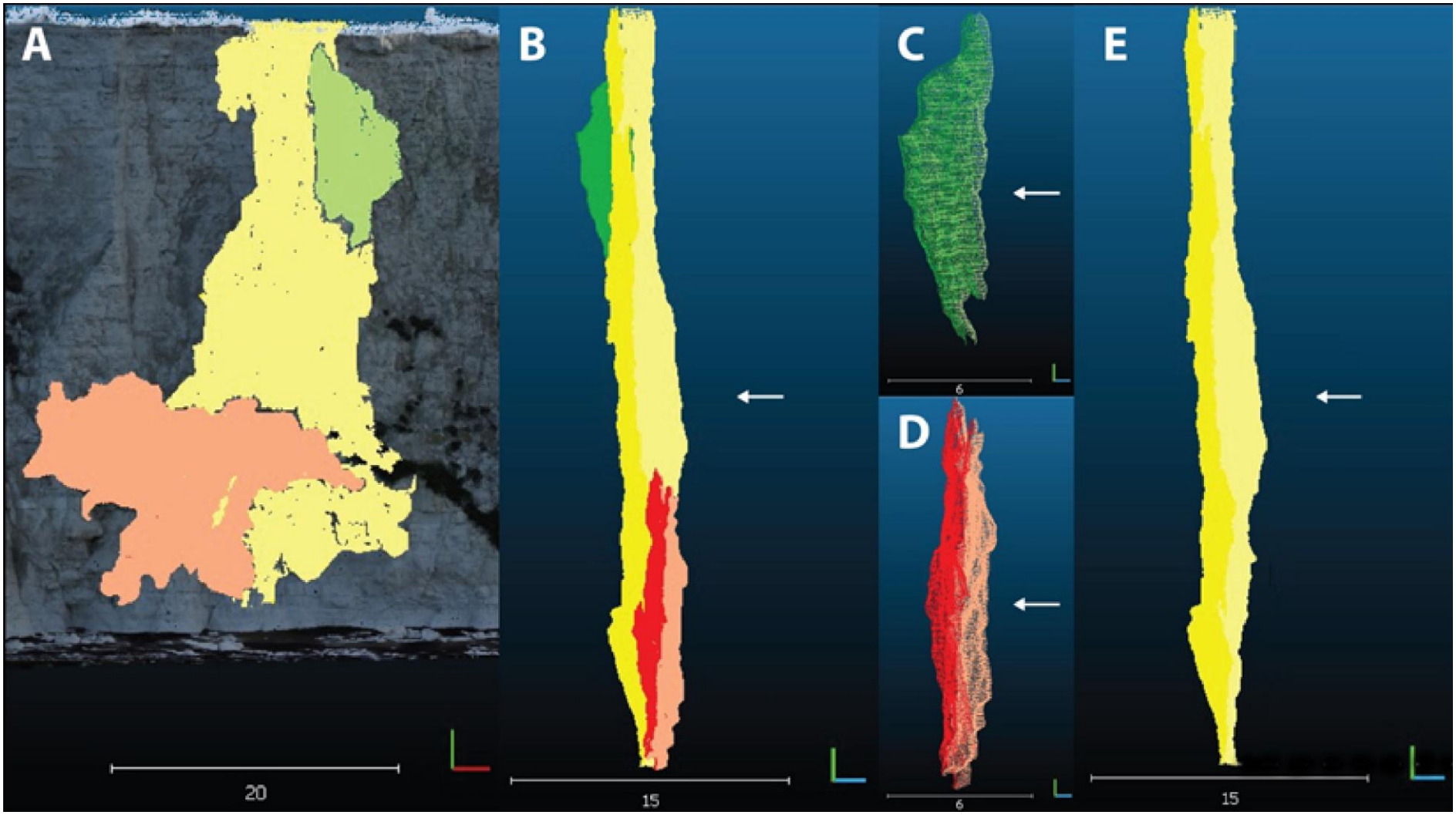

Figure 7: 3D models in Cloud Compare of successive block failures in the Newhaven Chalk at Telscombe between August and December 2016 (A) All three block failures with cliff point cloud, (B) Three blocks isolated side view looking west to east, (C) Oct-Nov failure, (D) Aug-Sep failure, (E) Nov-Dec failure [All scale bar measurements are in metres, arrows identify cliff face, lighter colours indicate surface before failure with darker representing post failure surface].

311 6. Using Cloud Compare (Cloud Compare v2.6.3, 2016) these blocks were isolated to provide a 3D
312 presentation of each failure (Figures 5C, 5D & 5E). The visualisation of these blocks can be compared
313 to that presented by Mortimore et al. (2004) who stated that after an initial block failure (Figure 7D),
314 further failures are likely to occur either in similar blocks observed on the cliff face (Figure 7C) or blocks
315 that exist deeper within the rock mass (Figure 7E). The series of failures observed confirm that the
316 initial failures led to a destabilisation in the cliff along the planes of weakness as presented by
317 Mortimore et al. (2004).

318 **4.2. Toe erosion and subsequent failure (August 2016 – March 2017)**

319 Approximately 55 m to the west of the presented successive failures monthly toe erosion was
320 detected totalling 104.9 m^3 between August 2016 and February 2017 (Figure 4 – 538863.09 m –
321 Easting, from 2.50 m to 13.28 m – Elevation). This well-established process of cliff failure led to the
322 largest observed failure in February-March 2017 of 2546.8 m^3 (Figure 4 – 538860.37 m – Easting, 30.07
323 m – Elevation). This figure is most likely an underestimate of the true volume due to the substantial
324 debris, which obscures the lower quarter of the cliff. Figure 8 illustrates, through 2.5D surface change
325 detection, the months with the largest precursor failures and Table 2 provides a monthly volumetric
326 breakdown of the observed erosion. The erosion to the right of the images (east) is not included in
327 these totals as it is representative of the arch erosion quantified in the previous section.

Month	Total volume of erosion within area of interest (m^3)	Average thickness of rockfall(s) (m)	Figure
August – September 2016	2.8	0.47	-
September – October 2016	0.6	0.27	-
October – November 2016	54.0	0.71	8A
November – December 2016	26.5	0.45	8B
December 2016 – January 2017	22.7	0.42	8C
January – February 2017	2.7	0.15	-
February – March 2017	2546.8	2.69	8D
TOTAL	**2656.1**		

328 Table 2: Volume of monthly toe erosion and the subsequent failure between August 2016 and March 2017.

Analysis of the 3D model following the largest failure revealed a conjugate joint set (Figure 9A)

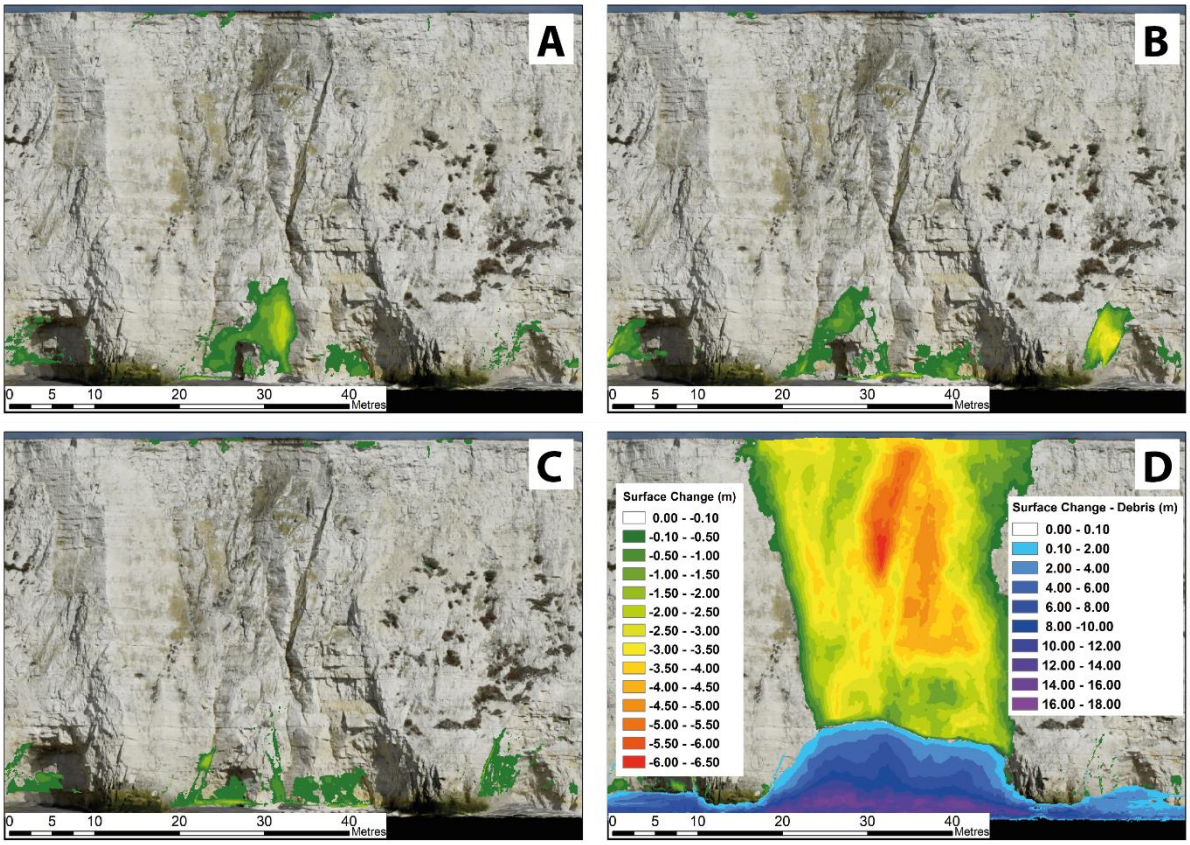

Figure 8: Surface change monitoring toe erosion and subsequent failure in the Newhaven Chalk at Telscombe, cell size=0.10 m (A) Oct-Nov 2016, (B) Nov-Dec 2016, (C) Dec 2016-Jan 2017, (D) Feb-Mar 2017.

intersecting at the base of cliff which formed a wedge. The kinematic analysis undertaken by Barlow et al. (2017) identified this mechanism of failure to be the most likely within the Newhaven Chalk at Telscombe. A limit equilibrium analysis (Figure 9B) was completed in the software Swedge to assess the impact of the steepening cliff face due to toe erosion. Figure 9C details the input parameters used for this analysis. The Factor of Safety (FoS) reduced from 1.51 to 1.00 between August 2016 and March 2017 (Figure 10) under these conditions (Figure 9C). The greatest reduction in FoS, as expected, coincided with the largest preceding failure of 54.0 m^3, this increased the cliff face angle by 2.74° to 78.77°. This failure along with those observed between August and February were focussed at the toe of the cliff where the conjugate joints intersected. The steepening of the cliff face would have increased the stress network along these planes of weakness within the chalk which primed this location to failure. During the 18 days between the February and March surveys there were several

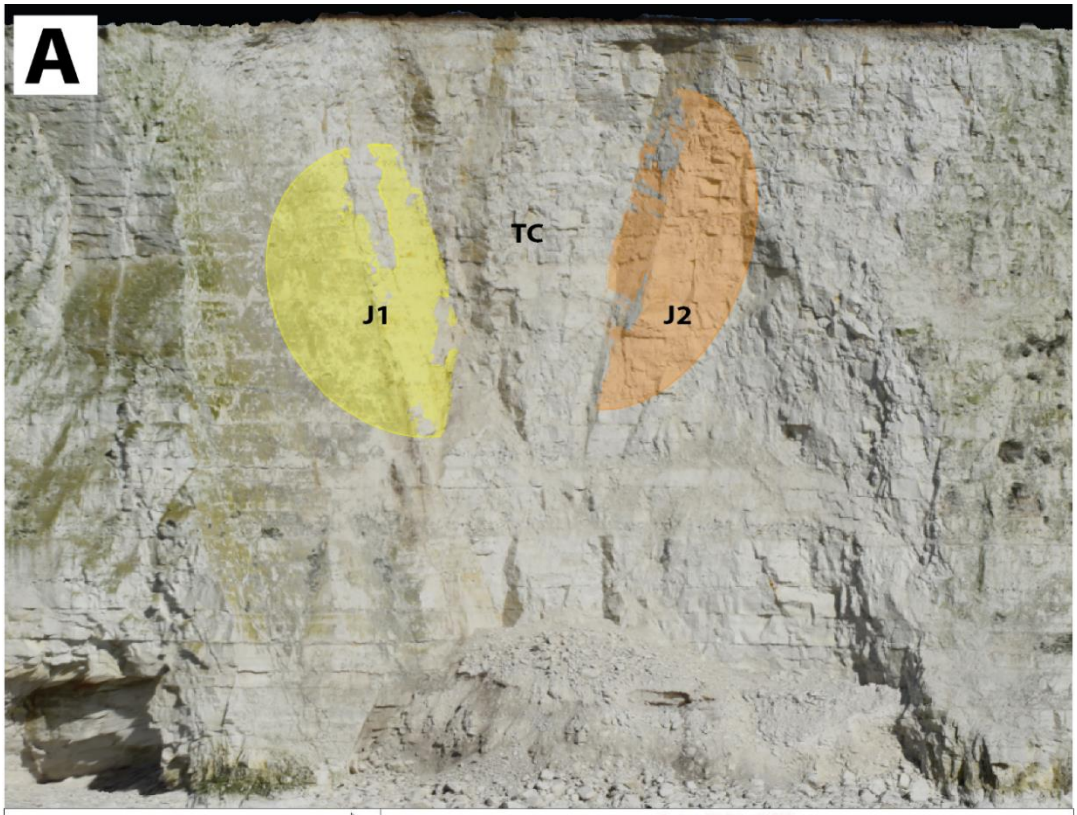

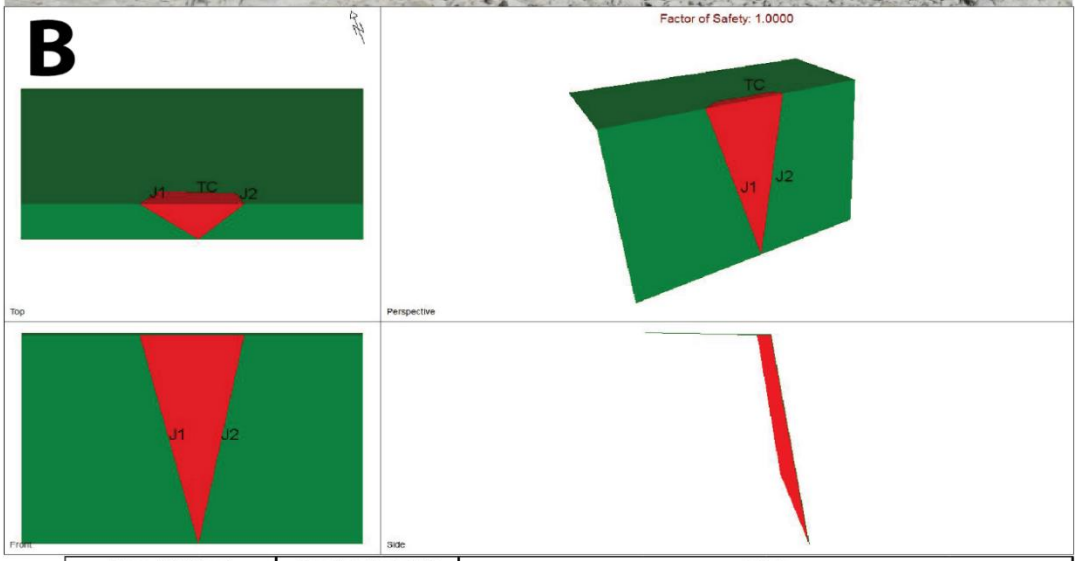

C

Slope (Cliff face)		Tension Crack (TC)		Joints			
Dip	80.43°	Dip	81.67°	Joint 1 (J1)		Joint 2 (J2)	
Dip direction	200.2°	Dip direction	201.57°	Dip	74.07°	Dip	75.27°
Height	41.83m	Trace length	4.41m	Dip direction	165.51°	Dip direction	253.43°
				Waviness	0°	Waviness	0°
Upper face							
Dip	1°			Shear strength model	Mohr-Coulomb	Shear strength model	Mohr-Coulomb
Dip direction	200.2°						
				cohesion (c)	23.044 kPa	cohesion (c)	23.044 kPa
Unit weight	16 kN/m^3			angle of friction (ϕ)	38°	angle of friction (ϕ)	38°

Figure 9: Limit equilibrium model of wedge failure between February and March 2017 using Swedge, (A) 3D model in ADAM 3DM Analyst detailing the joint surfaces, (B) Model output from Swedge, (C) Tabulated input parameters for Swedge analysis.

341 periods of strong winds that coincided with high tides. The Brighton Marina meteorological station

342 recorded the peak gust 21.6 ms^{-1} on the 23rd February 2017, and recorded the highest average wind

speed and average gust for the duration between surveys of 5.4 ms^{-1} and 7.25 ms^{-1} respectively. This would have led to substantial wave attack at the cliff toe which had been significantly eroded over the previous months.

4.3. Negative power law scaling parameters

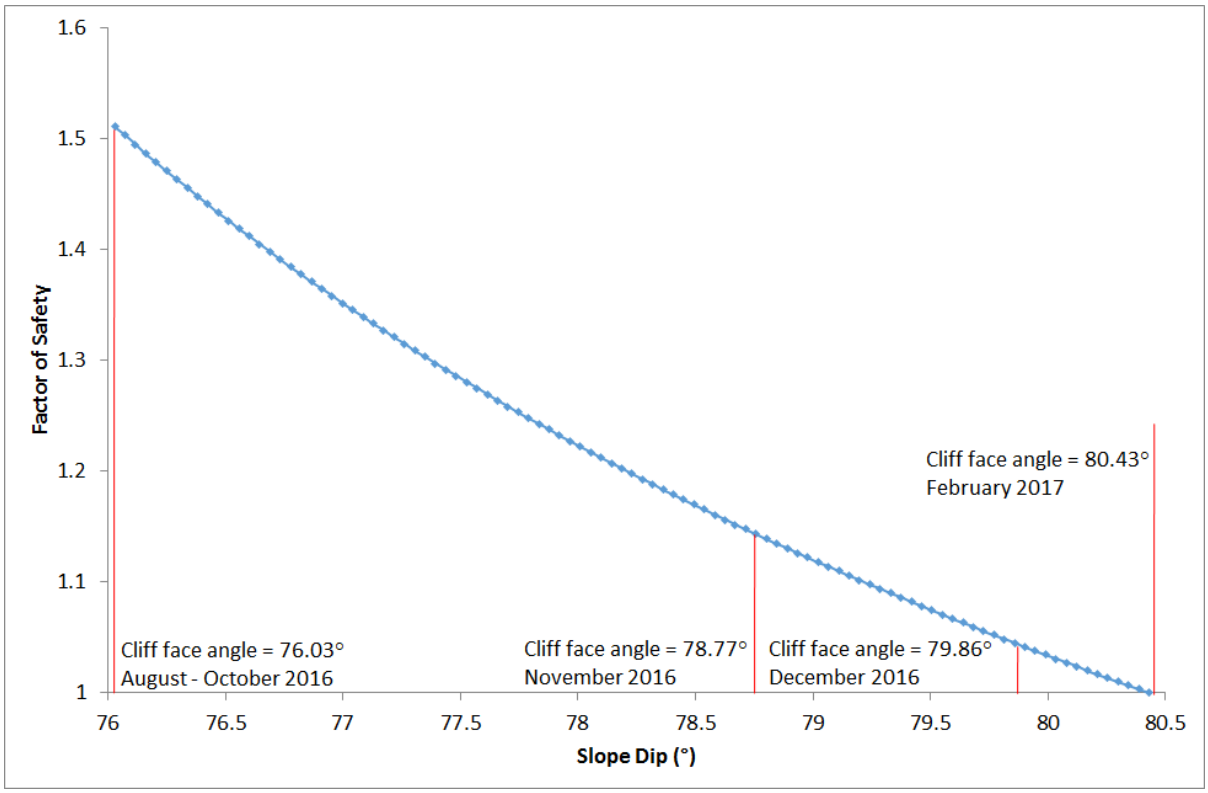

Figure 10: Limit equilibrium analysis of wedge failure in Newhaven Chalk, Telscombe effect of toe erosion in steepening of cliff face on Factor of Safety (FoS) using Swedge between August 2016 and February 2017.

As detailed by Barlow et al. (2012) the s value provides an indication on the level of activity within a given dataset whereas β describes the contribution of each magnitude of rockfall to the total volume. For example as β increases the smaller magnitude rockfalls contribute a greater amount to the total volume than the larger magnitude failures. The normalised scaling parameters for the study area varied between 1.421 to 1.955 for β and from 33.79 to 904.14 for s. The range in β values is consistent with those presented in other scientific research (Van Den Eeckhaut et al., 2007; Brunetti et al., 2009; Barlow et al., 2012). The smaller β and larger s values are generally found in the winter months (winter ave. β=1.557, ave. s=543.38, summer ave. β=1.820, ave. s=215.45) (Figure 11) when an increase in erosion would be expected due to the frequency of storms, with the exception of the

August to September record (β=1.592, s=544.82). With regards to the maximum failure volume (V_{max}), this is primarily controlled by the slope morphology (Martin et al., 2002). This is evidenced by the wedge failures at the site (Mortimore et al., 2004; Barlow et al., 2017) which constrain the magnitude of the observed larger failures in the inventory presented. Using these data, Gilham et al. (2018) found that the power law scaling parameters (β and s) are correlated to Hs at Telscombe and developed a probabilistic recession model based on the UK Climate Change Projection (UKCP) 2009 medium emission scenario.

5. Conclusions

Our research has demonstrated the benefits of deploying UAV photogrammetry for high precision

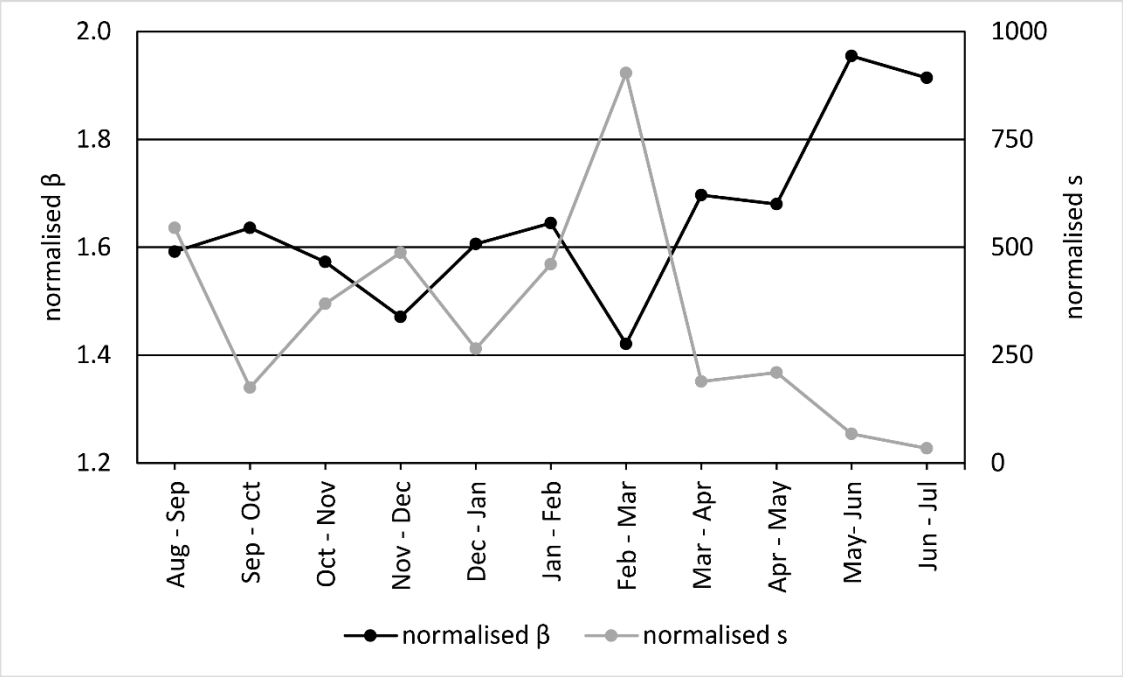

Figure 11: Monthly normalised β and s values from August 2016 to July 2017.

monitoring of the coastal cliff environment. Rapid data capture and models generated with comparable accuracy to TLS mean these complex environments are able to be captured and modelled much more efficiently than in previous research projects (Rosser et al., 2005; Lim et al., 2010). Due to the high frequency of data capture, precursors to larger failures were identified and illustrated the primary geological control of the Newhaven Chalk formation presented by Mortimore et al. (2004). The methodology presented provides an opportunity to assess the cliff throughout the erosional cycle.

This was evidenced with the limit equilibrium analysis of the slope, which showed the effect of a steepening cliff face, due to wave erosion, in the months preceding the largest failure within the study site. The 2.5D surface change detection methodology enabled automatic detection of rockfalls and significantly reduced processing time of the data and subsequent population of the rockfall inventory. However, before using this method an assessment of the surface of interest is required to determine the impact of estimating volumes from a single viewpoint. In this study, the impact of small changes in cliff azimuth on the volume of rockfalls was considered to be negligible. Through volumetric estimations and population of the monthly rockfall inventories, magnitude-frequency analysis using negative power laws showed strong correlations for the range of failure magnitudes. The methodology presented can be used for similar coastal cliff research projects or applied to other geomorphological environments to assess system change through time.

Acknowledgements

This research was funded through an EPSRC iCASE Studentship (Engineering and Physical Sciences Research Council Industrial Co-operative Award in Science and Engineering) through the University of Sussex with industrial collaboration from Halcrow Group Ltd (A CH2M Company) reference number: EP/L505687/1.

References

ADAM Technology. (2010). *3DM Analyst Mine Mapping Suite: 3D Measurement, Camera Calibration and Block Adjustment Software (First Edition, revision 1.0.137*). Belmont, Australia: ADAM Technology.

Bak, P. (1996). *How nature works: the science of self-organized criticality*. New York: Springer

Barlow, J., Gilham, J., & Cofrã, I. I. (2017). Kinematic analysis of sea cliff stability using UAV photogrammetry. *International Journal of Remote Sensing*. DOI: 10.1080/01431161.2016.1275061

Barlow, J., Lim, M., Rosser., N; Petley, D., Brain, M., Norman, E., & Geer, M. (2012). Modelling cliff erosion using negative power law scaling of rock falls. *Geomorphology*, 139-140, pp. 416-424. DOI: 10.1016/j.geomorph.2011.11.006

Birch, J. S. (2009). *3DM Analyst Mine Mapping Suite Training* [ADAM Technology Presentation]. Retrieved from: http://slideplayer.com/slide/6869698/

Brardinoni, F., & Church, M. (2004). Representing the landslide magnitude–frequency relation: Capilano River Basin, British Columbia. *Earth Surface Processes and Landforms*, 29(1), pp. 115–124. DOI: 10.1002/esp.1029

Brunetti, M. T., Guzzetti, F., & Rossi, M. (2009). Probability distributions of landslide volumes. *Nonlinear Processes in Geophysics*, 16(2), pp. 179-188. DOI: 10.5194/npg-16-179-2009

Buckley, S. J., Howell, H. D., Enge, H. D., & Kurz, T. H. (2008). Terrestrial laser scanning in geology: data acquisition, processing and accuracy considerations. *Journal of the Geological Society*, 165, pp. 625-638. DOI: 10.1144/0016-76492007-100

Channel Coastal Observatory (CCO). (2015). *Channel Coastal Observatory - Regional Coastal Monitoring Programmes Seaford Wave Buoy*. Retrieved from http://www.channelcoast.org/data_management/real_time_data/charts/?chart=81&tab=info&disp_option=

Clifford, J. M., Förstner, W., Bernhard, W., Paderes, F., & Munjy, R. (2004). The mathematics of photogrammetry. In J. McGlone, E. Mikhail, & R. Mullen (Eds.), *Manual of photogrammetry* (pp. 181-316) (5th ed.). Maryland: American Society of Photogrammetry and Remote Sensing.

Cloud Compare v2.6.3. (2016). *CloudCompare 3D point cloud and mesh processing software Open Source Project*. Retrieved from http://www.cloudcompare.org/

Cook, K. L. (2017). An evaluation of the effectiveness of low-cost UAVs and structure from motion for geomorphic change detection. *Geomorphology*, 278, pp. 195-208. [Online] DOI: 10.1016/j.geomorph.2016.11.009

Dewez, T. J. B., Rohmer, J., Regard, V., & Cnudde, C. (2013). Probabilistic coastal cliff collapse hazard from repeated terrestrial laser surveys: case study from Mensil Val (Normandy, northern France). *Journal of Coastal Research*, Special Issue 65 – International Coastal Symposium Volume 1, pp. 702-707. [Online] DOI: 10.2112/SI65-119.1

Dewez, T.J.B., Leroux, J., & Morelli, S. (2016) Cliff collapse hazard from repeated multicopter UAV acquisitions: return on experience, Int. Arch. Photogramm. Remote Sens. Spatial Inf. Sci., XLI-B5, 805-811, doi:10.5194/isprs-archives-XLI-B5-805-2016

Di Mario, R. (2006). Evaluation of sixteen years of INGV seismic bulletins. *Annals of Geophysics*, 49(2-3), pp. 853-865. [Online] DOI: 10.4401/ag-3120

Dong, P., & Guzzetti, F. (2005). Frequency-size statistics of coastal soft-cliff erosion. *Journal of Waterway, Port, Coastal, and Ocean Engineering,* 131(1), pp. 37-42.

Dussauge, C., Grasso, J.-R., & Helmstetter, A. (2003). Statistical analysis of rock fall volume distributions: implications for rock fall dynamics. *Journal of Geophysical Research*, 108(B6), 2286. DOI: *10.1029/2001JB000650*

Eisenbeiβ, H. (2009). *UAV Photogrammetry* (Unpublished doctoral Thesis). University of Technology Dresden, Zurich. Retrieved from www.igp-data.ethz.ch/berichte/blaue_berichte_pdf/105.pdf

436 Fraser, C. S., & Cronk, S. (2009). A hybrid measurement approach for close-range photogrammetry.
437 *ISPRS Journal of Photogrammetry and Remote Sensing*, 64(3), pp. 328-333. DOI:
438 10.1016/j.isprsjprs.2008.09.009

439 Gilham, J., Barlow, J., & Moore, R. (2018). Marine control over negative power law scaling of mass
440 wasting events in chalk sea cliffs with implications for future recession under the UKCP09
441 medium emission scenario. *Earth Surface Processes and Landforms*, 43 (10), pp 2136-2146.
442 DOI: 439 10.1002/esp.4379

443 Glennie, C. L., Carter, W. E., Shrestha, R. L., & Dietrich, W. E. (2013). Geodetic imaging with airborne
444 LiDAR: the Earth's surface revealed. *Reports on Progress in Physics*, 76(8), 086801.

445 Gonçalves, J. A., & Henriques, R. (2015). UAV photogrammetry for topographic monitoring of coastal
446 areas. *ISPRS Journal of Photogrammetry and Remote Sensing*, 104, pp. 101-111. DOI:
447 10.1016/j.isprsjprs.2015.02.009

448 Graham, R., & Koh, A. (2002). *Digital Aerial Survey: Theory and Practice*. Caithness, Scotland:
449 Whittles Publishing.

450 Guthrie, R., & Evans, S. (2004). Analysis of landslide frequencies and characteristics in a natural
451 system. Coastal British Columbia. *Earth Surface Processes and Landforms*, 29(11), pp. 1321–
452 1339. DOI: 10.1002/esp.1095

453 Haala, N., & Rothermel, M. (2012). Dense Multi-Stereo Matching for High Quality Digital Elevation
454 Models. *PFG Photogrammetrie-Fernerkundung-Geoinformation*, 2012(4), pp. 331-343. DOI:
455 10.1127/1432-8364/2012/0121

456 Hantz, D., Vengeon, J. M., & Dussauge-Peisser, C. (2003). An historical, geomechanical and
457 probabilistic approach to rock-fall hazards assessment. *Natural Hazards and Earth System*
458 *Science*, 3(6), pp. 693-701.

459 Hovius, N., Stark, C., & Allen, P. (1997). Sediment flux from a mountain belt derived by landslide
460 mapping. *Geology*, 25(3), pp. 231–234. DOI: 10.1130/0091-
461 7631(1997)025<0231:SFFAMB>2.3.CO;2

462 Huang, Y. D. (2000). Evaluation of information loss in digital elevation models with digital
463 photogrammetric systems. *The Photogrammetric Record*, 16(95), pp. 781-791. DOI:
464 10.1111/0031-868X.00151

465 Hugenholtz, C. H., Whitehead, K., Brown, O. W., Barchyn, T. E., Moorman, B. J., LeClair, A., Riddell, K.,
466 & Hamilton, T. (2013). Geomorphological mapping with a small unmanned aircraft system
467 (sUAS): Feature detection and accuracy assessment of a photogrammetrically-derived digital
468 terrain model. *Geomorphology*, 194, pp. 16-24. DOI:10.1016/j.geomorph.2013.03.023

469 Hurst, M. D., Rood, D. H., Ellis, M. A., Anderson, R. S., & Dornbusch, U. (2016). Recent acceleration in
470 coastal cliff retreat rates on the south coast of Great Britain. *Proceedings of the National*
471 *Academy of Sciences of the United States of America*, 113(47), pp. 13336-13341. DOI:
472 10.1073/pnas.1613044113

473 Hyyppä, J., Yu, X., Hyyppä, H., Vastaranta, M., Holopainen, M., Kukko, A., Kaartinen, H., Jaakkola, A.,
474 Vaaja, M., Koskinen, J., & Alho, P. (2012). *Remote Sensing*, 4(5), pp. 1190-1207. [Online] DOI:
475 10.3390/rs4051190

476 James, M. R., & Robson, S. (2012). Straightforward reconstruction of 3D surfaces and topography
477 with a camera: Accuracy and geoscience application. *Journal of Geophysical Research*, 117,
478 F03017, DOI: 10.1029/2011JF002289

479 James, M. R., & Robson, S. (2014). Mitigating systematic error in topographic models derived from
480 UAV and ground-based image networks. *Earth Surfaces Processes and Landforms*, 39(10), pp.
481 1413-1420. [Online] DOI: 10.1002/esp.3609

482 James, M. R., Robson, S., & Smith, M. W. (2017). 3-D uncertainty-based topographic change
483 detection with structure-from-motion photogrammetry: precision maps for ground control
484 and directly georeferenced surveys. *Earth Surface Processes and Landforms*, 42(12), pp. 1769-
485 1788. [Online] DOI: 10.1002/esp.4125

486 Konecny, G. (2003). *Geoinformation: remote sensing, photogrammetry and geographic information*
487 *systems* (1st ed.). London: Taylor & Francis.

488 Korup, O. (2005). Distribution of landslides in southwest New Zealand. *Landslides*, 2(1), pp. 43–51.
489 DOI: 10.1007/s10346-004-0042-0

490 Kuhn, D., & Prüfer, S. (2014). Coastal cliff monitoring and analysis of mass wasting processes with
491 the application of terrestrial laser scanning: A case study of Rügen, Germany. *Geomorphology*,
492 213, pp. 153-165. [Online] DOI: 10.1016/j.geomorph.2014.01.005

493 Lee, E. M. (2008). Coastal cliff behaviour: Observations on the relationship between beach levels and
494 recession rates. *Geomorphology*, 101(4), pp. 558-571. [Online] DOI: 10.1002/esp.3609

495 Lee., E. M., Hall, J. W., & Meadowcroft, I. C. (2001). Coastal cliff recession: the use of probabilistic
496 prediction methods. *Geomorphology*, 40(3-4), pp. 253-269. DOI: 10.1016/S0169-
497 555X(01)00053-8

498 Lim, M. (2006). *Coastal cliff evolution with reference to Staithes, North Yorkshire*. (Unpublished
499 doctoral Thesis). Durham University, Durham, UK. URL: http://etheses.dur.ac.uk/1809/

500 Lim, M. (2014). 'The rock coast of the British Isles: cliffs', in Kennedy, D. M., Stephenson, W. J., &
501 Naylor, L. A. (Eds.) *Rock Coast Geomorphology: A Global Synthesis*. London: Geological Society
502 Memoirs, 40, pp. 19-38.

503 Lim, M., Rosser, N. J., Allison, R. J., & Petley, D. N. (2010). Erosional processes in the hard rock
504 coastal cliffs at Staithes, North Yorkshire. *Geomorphology*, 114(1-2), pp. 12-21. DOI:
505 10.1016/j.geomorph.2009.02.011

506 Linder, W. (2003). *Digital Photogrammetry. Theory and Applications*. Berlin: Springer.

507 Luhmann, T., Robson, S., Kyle, S., & Boehm, J. (2013). *Close Range Photogrammetry and 3D Imaging*
508 (2nd ed.). Berlin: De Gruyter.

509 Lumme, J., Karjalainen, M., Kaartinen, H., Kukko, A., Hyyppä, H., Jaakkola, A., & Kleemola, J. (2008).
510 Terrestiral laser scanning of agricultural crops. *The International Archives of the*
511 *Photogrammetry, Remote Sensing and Spatial Information Sciences*, 37, pp. 563-566.

Malamud, B., Turcotte, D., Guzzetti, F., & Reichenbach, P. (2004). Landslide inventories and their statistical properties. *Earth Surface Processes and Landforms*, 29(6), pp. 687–711. DOI: 10.1002/esp.1064

Marques, F. M. S. F. (2008). Magnitude–frequency of sea cliff instabilities. *Natural Hazards and Earth System Sciences,* 8(5), pp. 1161–1171. DOI: 10.5194/nhess-8-1161-2008

Martin, Y., Rood, K., Schwab, J., & Church, M. (2002). Sediment transfer by shallow landsliding in the Queen Charlotte Islands, British Columbia. *Canadian Journal of Earth Sciences*, 39(2), pp. 189–205. DOI: 10.1139/e01-068

Matthews, N. A. (2008). *Aerial and close-range photogrammetric technology: providing resource documentation, interpretation, and preservation*. Technical Note 428. Denver, Colorado: Bureau of Land Management. Retrieved from *www.blm.gov/nstc/library/pdf/TN428.pdf*

May, V. J. (2003) – 'Beachy Head – Seaford Head Chapter 4: Soft Rock Cliffs' in May, V. J., & Hansom, J. D. *Coastal Geomorphology of Great Britain. Geological Conservation Review Series, No. 28*. Peterborough: Joint Nature Conservation Committee, 10.

Medjkane, M. Maquaire, O., Costa, S., Roulland, T, Letortu, P., Fauchard, C., Antoine, R., & Davidson, R. (2018). High-resolution monitoring of complex coastal morphology changes: cross-efficiency of SfM and TLS-based survey (Vaches-Noires cliffs, Normandy, France). *Landslides*, 15(6), pp. 1097-1108. [Online] DOI: 10.1007/s10346-017-0942-4

Michoud, C., Carrea, D., Costa, S., Derron, M., Jaboyedoff, M., Delacourt, C., Maquaire, O., Letortu, P., & Davidson, R. (2015). Landslide detection and monitoring capability of boat-based mobile laser scanning along Dieppe coastal cliffs, Normandy. *Landslides*, 12(2), pp. 403-418. [Online] DOI: 10.1007/s10346-014-0542-5

Mortimore, R. N. (1997). *The Chalk of Sussex and Kent*. London: The Geologists Association.

Mortimore, R. N., Lawrence, J., Pope, D., Duperret, A., & Genter, A. (2004). 'Coastal cliff geohazards in weak rock: the UK Chalk cliffs of Sussex', in Mortimore, R. N., & Duperret, A. (Eds.) *Coastal Chalk Cliff Instability*. London: Geological Society, Engineering Geology Special Publications, pp. 3-32.

Remondino, F., & El-Hakim, S. (2006). Image-based 3D modelling: a review. *The Photogrammetric Record*, 21(115), pp. 269-291. DOI: 10.1111/j.1477-9730.2006.00383.x

Rosser, N. J., Petley, D. N., Lim, M., Dunning, S. A., & Allison, R. J. (2005). Terrestrial laser scanning for monitoring the process of hard rock coastal cliff recession. *Quarterly Journal of Engineering Geology and Hydrogeology*, 38, pp. 363-375. DOI: 10.1144/1470-9236/05-008

Rossi, M., Witt, A., Guzzetti, F., Malamud, B., & Peruccacci, S. (2010). Analysis of historical landslide time series in the Emilia-Romagna region, northern Italy. *Earth Surface Processes and Landforms*, 35(10), pp. 1123–1137. DOI: 10.1002/esp.1858

Stark, C., & Guzzetti, F. (2009). Landslide rupture and probability distribution of mobilized debris volumes. Journal of *Geophysical Research*, 114(F2), pp. F00A02. DOI: 10.1029/2008JF001008

Stark, C., & Hovius, N. (2001). The characterization of landslide size distributions. *Geophysical Research Letters*, 28(6), pp. 1091–1094. DOI: 10.1029/2000GL008527

551 Teixeira, S. B. (2006). Slope mass movements on rocky sea-cliffs: A power-law distributed natural
552 hazard on the Barlavento Coast, Algarve, Portugal. *Continental Shelf Research*, 26(9), pp. 1077-
553 1091. DOI: 10.1016/j.csr.2005.12.013

554 Trenhaile, A. S. (2002). Rock coasts, with particular emphasis on shore platforms. *Geomorphology*,
555 48(1-3), pp. 7-22. DOI: 10.1016/S0169-555X(02)00173-3

556 Van Den Eeckhaut, M., Poesen, J., Govers, G., Verstraeten, G., & Demoulin, A. (2007). Characteristics
557 of the size distribution of recent and historical landslides in a populated hilly region. *Earth and*
558 *Planetary Science Letters*, 256(3-4), pp. 588–603. DOI: 10.1016/j.epsl.2007.01.040

559 Wenzel, K., Rothermel, M., Fritsch, D., & Haala, N. (2013). Image acquisition and model selection for
560 multi-view stereo. *International Archives of the Photogrammetry, Remote Sensing and Spatial*
561 *Information Sciences*, Volume XL-5/W1, pp. 251-258. [Online] DOI: 10.5194/isprsarchives-XL-5-
562 W1-251-2013

563 Westoby, M. J., Brasington, J., Glasser, N. F., Hambrey, M. J., & Reynolds, J. M. (2012). 'Structure-
564 from-Motion' Photogrammetry: A Low Cost, Effective Tool for Geoscience Applications.
565

566 White, E. P., Enquist, B. J., & Green, J. L. (2008). On estimating the exponent of power law frequency
567 distributions. *Ecology*, 89(4), pp. 905–912. DOI: 10.1890/07-1288.1

568 Wolman, M. G., & Miller, J. P. (1960). Magnitude and frequency of forces in geomorphic processes.
569 *Journal of Geology*, 68(1), pp. 54-74. DOI: 10.1086/626637

570 Young, E. J. (2012). dGPS. In S. J. Cook, L. E. Clarke, & J. M. Nield (Eds.), *Geomorphological Techniques*
571 (ISSN 2047-0371, pp.1-10). Retrieved from:
572 http://www.geomorphology.org.uk/geomorph_techniques

573